AGU ADVANCING EARTH AND SPACE SCIENCE

Geophysical Research Letters®

RESEARCH LETTER
10.1029/2022GL100149

Special Section:
Southern Ocean and Climate: Biogeochemical and Physical Fluxes and Processes

Atmospheric Rivers Contribute to Summer Surface Buoyancy Forcing in the Atlantic Sector of the Southern Ocean

Johan M. Edholm[1], Sebastiaan Swart[1,2], Marcel D. Plessis[1,3], and Sarah-Anne Nicholson[3]

[1]Department of Marine Sciences, University of Gothenburg, Gothenburg, Sweden, [2]Department of Oceanography, University of Cape Town, Rondebosch, South Africa, [3]Southern Ocean Carbon-Climate Observatory (SOCCO), CSIR, Cape Town, South Africa

Key Points:

- Atmospheric rivers (ARs) significantly increase precipitation (189%) in midlatitude cyclones over the Atlantic Southern Ocean
- During intense AR-driven rainfall events, precipitation contributes to daily buoyancy forcing equivalent to the surface heat flux
- Precipitation associated with ARs contributes cumulatively to 10% of the surface ocean buoyancy gain in summer

Supporting Information:

Supporting Information may be found in the online version of this article.

Correspondence to:

J. M. Edholm,
johan.edholm@gu.se

Citation:

Edholm, J. M., Swart, S., Plessis, M. D., & Nicholson, S.-A. (2022). Atmospheric rivers contribute to summer surface buoyancy forcing in the Atlantic sector of the Southern Ocean. *Geophysical Research Letters*, *49*, e2022GL100149. https://doi.org/10.1029/2022GL100149

Received 30 JUN 2022
Accepted 24 AUG 2022

Author Contributions:

Conceptualization: Sebastiaan Swart
Data curation: Johan M. Edholm, Sarah-Anne Nicholson
Formal analysis: Johan M. Edholm
Funding acquisition: Sebastiaan Swart, Marcel D. Plessis, Sarah-Anne Nicholson
Investigation: Johan M. Edholm

Abstract Atmospheric rivers (ARs) dominate moisture transport globally; however, it is unknown what impact ARs have on surface ocean buoyancy. This study explores the surface buoyancy gained by ARs using high-resolution surface observations from a Wave Glider deployed in the subpolar Southern Ocean (54°S, 0°E) between 19 December 2018 and 12 February 2019 (55 days). When ARs combine with storms, the associated precipitation is significantly enhanced (189%). In addition, the daily accumulation of AR-induced precipitation provides a buoyancy gain to the surface ocean equivalent to warming by surface heat fluxes. Over the 55 days, ARs accounted for 47% of the total precipitation equating to 10% of the summer surface ocean buoyancy gain. This study indicates that ARs play an important role in the summer precipitation over the subpolar Southern Ocean and that they can alter the upper-ocean buoyancy budget from synoptic to seasonal timescales.

Plain Language Summary Atmospheric rivers (ARs) are river-like features in the sky that carry enormous amounts of water vapor from the tropics toward Antarctica and across the Southern Ocean. However, it is not well documented how this freshwater carried by ARs in the atmosphere impacts rainfall over the ocean. This study uses an uncrewed surface vehicle, called a Wave Glider, to measure the meteorology and surface ocean temperature and salinity. We show that ARs almost double rainfall, which directly impact the surface ocean buoyancy (i.e., rainfall adds freshwater and lightens the surface layer waters). These results provide evidence and highlight the importance of ARs in the Atlantic Southern Ocean when it comes to lightening the surface waters.

1. Introduction

Atmospheric rivers (ARs) are narrow bands of elevated water vapor fluxes typically associated with the low-level atmospheric jet, located in the lower 3 km of the atmosphere (Ralph et al., 2017). They are transient features and despite covering only 10% of Earth's surface area, they account for 90% of poleward water vapor transport (Nash et al., 2018; Zhu & Newell, 1998). ARs often feature ahead of an extratropical cyclone's cold front and within the cyclone's warm conveyor belt. In the Eastern Pacific, 82% of ARs are connected to a midlatitude cyclone (storm), while only 45% of storms are paired with an AR (Zhang et al., 2019). AR presence could impact the storm dynamics due to the close connection between cold fronts and ARs over the Southern Ocean (Simmonds et al., 2012). Simmonds et al. (2012) found that these cold fronts strengthen the Subantarctic cyclone dynamics and that the fronts appear with the highest frequency between 40°S and 60°S with typical lengths of 2,000 km. The climatic importance of ARs, which stretch across the Atlantic Ocean from the Subtropics to the Antarctic continent, is starting to be realized. For instance, ARs have been shown to greatly impact precipitation patterns in the Western Cape of South Africa via a poleward migration of the moisture track (Blamey et al., 2018; Sousa et al., 2018), reduce high-latitude Antarctic sea-ice concentrations and expanse (Wille et al., 2021), and contribute to the opening of the Weddell Sea polynya (Francis et al., 2020). One area that remains unexplored to date is the potential impact ARs have on precipitation magnitudes over the ocean and the associated change in the surface ocean buoyancy.

Southern Ocean surface buoyancy fluxes are crucial to understanding climate due to their role in ocean ventilation and water-mass modification (Abernathey et al., 2016; Marshall & Speer, 2012; Pellichero et al., 2018). South of the Polar Front, deep waters upwell to the surface where they are exposed to surface fluxes of heat (solar radiation) and freshwater (sea-ice melt and precipitation). Abernathey et al. (2016) showed that sea-ice formation/melt and freshwater flux from precipitation played a critical role in lowering the density of upwelled waters,

Methodology: Johan M. Edholm, Sebastiaan Swart, Marcel D. Plessis, Sarah-Anne Nicholson
Project Administration: Sebastiaan Swart
Resources: Johan M. Edholm, Sebastiaan Swart, Sarah-Anne Nicholson
Supervision: Sebastiaan Swart, Marcel D. Plessis, Sarah-Anne Nicholson
Validation: Sarah-Anne Nicholson
Visualization: Johan M. Edholm, Marcel D. Plessis, Sarah-Anne Nicholson
Writing – original draft: Johan M. Edholm
Writing – review & editing: Johan M. Edholm, Sebastiaan Swart, Marcel D. Plessis, Sarah-Anne Nicholson

aiding in driving meridional overturning circulation (open ocean precipitation south of 50°S adds 24.2 km^3 freshwater to the ocean every day, compared to 43.2 km^3 from sea-ice melt). Further, precipitation over the ocean can create surface "rain lenses," which are very shallow layers with a reduced salinity (ten Doeschate et al., 2019; Shcherbina et al., 2019; Iyer & Drushka, 2021). These layers are highly stratified and therefore suppress turbulence close to the surface, which in turn could inhibit the transfer of turbulent energy from the surface to the deeper parts of the mixed layer (Iyer & Drushka, 2021). Given that ARs are predicted to increase in frequency and carry more moisture over the ocean due to anthropogenic warming (Payne et al., 2020), understanding how they currently impact surface ocean buoyancy is an important step toward quantifying the impact ARs will have on the surface ocean and its circulation in the future.

In this study, we identify ARs over the Atlantic sector of the Southern Ocean using reanalysis data sets and determine their associated water vapor transport and precipitation. We then use multimonth Wave Glider observations from 54°S, 0°E to investigate in detail the link between precipitation related to ARs and the summer surface ocean buoyancy variability. In addition, we discuss the caveats of analyzing a Lagrangian process in an Eulerian framework and contextualize the findings concerning water mass transformation in the Southern Ocean.

2. Data and Methods

2.1. Field Data Sets and Reanalysis Products

A Liquid Robotics Wave Glider (WG), a wave-propelled uncrew surface vehicle, was deployed in the Southern Ocean during austral summer (19 December 2018–12 February 2019, 55 days) at 54°S, 0°E (Figure 1) as part of the SOSCEx-STORM2 experiment (Southern Ocean Seasonal Cycle Experiment; Swart et al., 2012). The WG sampled in a figure of eight pattern with a meridional length of 20 km and a zonal width of 5 km (Figure 1c). Meteorology measurements (true wind speed and direction, barometric pressure, and air temperature) were made with an Airmar WX-200 Ultrasonic Weather Station (Schmidt et al., 2017), attached to the WG at 0.7 m height above sea level. The WG was also equipped with a SeaBird Glider Payload CT-cell, measuring temperature and conductivity of the surface ocean (0.3 m below the surface). Both sensors have a sample rate of 1 Hz, which are averaged into 20-min bins for further analysis.

The variability of surface ocean salinity, observed by the WG, is used to document the surface ocean response to freshwater input from precipitation; thus, reliable estimates of salinity are important. However, high wind events cause surface turbulence, likely leading to air bubbles suspended in the water that enters the CT-cell resulting in periodic decreases in salinity seen on the order of >1 g kg^{-1} between consecutive measurements (Figure S1 in Supporting Information S1). We isolated these spikes by comparing changes between time steps (dS), and if two adjacent values in dS are greater than the 95th percentile of dS, and the opposite sign, we remove the associated value in salinity. As expected, periods of high wind (>15 m s^{-1}) with the likely increase in surface turbulence and bubble production (Figure S1c in Supporting Information S1) correlate well with the isolated occurrences of salinity outliers (Figure S1b in Supporting Information S1) and the "noisy" periods of processed salinity data (Figures S1d and S1e in Supporting Information S1). Lastly, a Savitsky-Golay filter is applied to the data; this method fits a low-order polynomial to a rolling window of the time series, effectively smoothing the data (Savitzky & Golay, 1964). This post-processing of the data was done using the Python GliderTools package of Gregor et al. (2019).

To evaluate ARs, storms, and precipitation, we use ERA5 reanalysis variables. ERA5 is the fifth-generation atmospheric reanalysis of global climate from The European Center for Medium Range Weather Forecasting (ECMWF, see Hersbach et al., 2020 for more detail). This product is available hourly, at several heights (1,000–300 hPa), and at a spatial resolution of 1/4° or ∼27 km (for ARs, it is downsampled to 6 hr and 0.75° resolution, like the 1° by Wille et al., 2021). We calculate freshwater fluxes from precipitation and evaporation, where positive values indicate that the ocean is gaining freshwater (i.e., buoyancy). For simplicity's sake, we will refer to total precipitation (tp) as the net freshwater gain/loss ($P - E$) as evaporation is one order of magnitude smaller ($P = 0.11 \pm 0.26$ mm compared to $E = 0.02 \pm 0.03$ mm).

Previous studies using autonomous surface vessels in the Southern Ocean have showed that the ECMWF reanalysis products were the most accurate in representing the temporal variability of winds, when compared with observations made by WGs (ERA-Interim—Schmidt et al., 2017) and a Sailbuoy (ERA5—Swart et al., 2020).

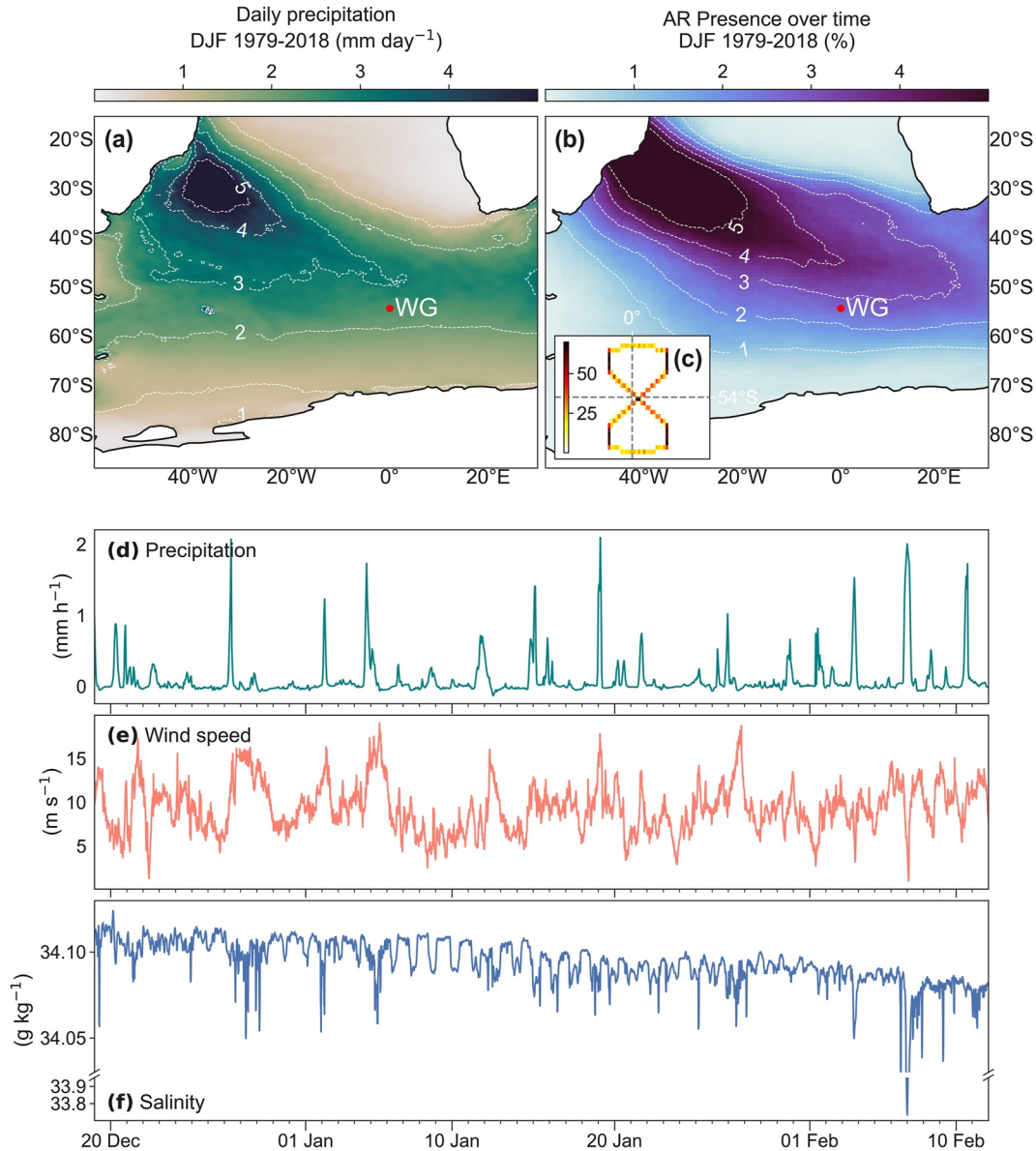

Figure 1. (a) Austral summer climatology (DJF, 1979–2018) of (a) daily precipitation and (b) atmospheric river distribution in time and space, derived from ERA5. The location of the Wave Glider (WG) deployment is marked in both (a and b). (c) Distribution (heat map) of the WG sampling pattern ($n = 3{,}960$). (d) ERA5 hourly precipitation ($P - E$) at the location of the WG. Time series ($dt = 20$ min) of near-surface (0.5 m) wind speed (e) and absolute salinity (f) measured at the surface (0.3 m depth) by the WG during austral summer in 2018–2019. Note the break in the y axis for the salinity magnitude.

Further, du Plessis et al. (2022) show no significant difference in the summer mixed-layer buoyancy gain of the Southern Ocean when calculated using ERA5 and two other commonly used reanalysis products.

2.2. Buoyancy Calculations

To understand the impact of rainfall events and associated freshwater input on the surface ocean buoyancy, we compute the buoyancy flux through the surface (B):

$$B = \frac{g \cdot \alpha_T}{c_w \cdot \rho_{\text{ref}}} \cdot Q_{\text{NET}} + g \cdot \beta_S \cdot S \cdot (E - P), \quad (1)$$

where ρ_{ref} is the reference density, α_T is the thermal expansion coefficient, c_W is the specific heat for sea water, Q_{NET} is net heat flux across the surface obtained from the ERA5 reanalysis product (see Section 2.1 for details) colocated to the time and position of the WG, β_S is the haline contraction coefficient, S is the WG observed salinity, and $(E - P)$ is evaporation minus precipitation, also taken from the ERA5 reanalysis. B consists of a thermal (with Q_{NET}) and haline (with S and $[E - P]$) contribution.

The net heat flux through the surface (Q_{NET}) is determined by

$$Q_{NET} = Q_{LW} + Q_{SW} + Q_{LH} + Q_{SH}, \tag{2}$$

where Q_{LW} is the longwave radiation, Q_{SW} is the shortwave radiation, Q_{LH} is the latent heat flux, and Q_{SH} is the sensible heat flux. Positive Q_{NET} depicts the ocean gaining heat.

2.3. Identification of ARs and Storms

To determine the presence of ARs, we calculate integrated water vapor transport (IVT) by integrating the product of specific humidity (q), a mass fraction of kgs water per kg air, and wind speed (u and v) from the surface to around 10,000 m (300 hPa) (Zhu & Newell, 1998). IVT is calculated according to

$$\mathrm{IVT} = \frac{1}{g}\int_{p_0}^{300\mathrm{hPa}} qV\,\mathrm{d}p, \tag{3}$$

where g is the gravitational acceleration, p_0 is the pressure at the surface (1,000 hPa), q and V are specific humidity (g kg^{-1}) and the vector wind (m s^{-1}) at the given pressure level, respectively, and dp is the difference between adjacent pressure levels. We determine ARs for the summer months only (December–February, DJF) between 1980 and 2019. We subsample the original data set to every 6 hr on a 3/4° grid in accordance with multiple AR studies (see Shields et al., 2018 for a cohesive summary of detection methods and their outputs). We use the method described by Guan and Waliser (2015) to identify ARs. For every month in the ERA5 data set, we identify regions of high IVT, above which the 85th percentile for each grid cell for a 5-month period centered on that month and a fixed lower limit of 150 kg m^{-1} s^{-1} are also imposed and have a meridional component of a minimum of 50 kg m^{-1} s^{-1}. This is to ensure that the objects are moving toward the pole and not only being transported zonally. Contiguous regions of grid cells with IVT values above the threshold and the fixed lower limits are isolated, after which length, size, coherent direction, and mean meridional IVT criteria are applied, filtering out objects that do not meet all criteria.

To link precipitation and ARs to storms, we need to identify storms. We adapt the method of Cohen et al. (2017), where a major storm is classified by a decrease in sea level pressure by more than 5 hPa in 6 hr and 10-min winds stronger than 6 m s^{-1} for at least three consecutive hours with a maximum break of 1 hr. Any period with the same sea level pressure decrease and containing a period of high wind speed (>8 m s^{-1}) for at least 3 hr is classified as a storm. Similar to Wang et al. (2015), we associate precipitation 6 hr prior to and after a storm to that system, and if there are any overlapping periods, they are considered the same system.

3. Results

3.1. Summer Moisture Transport and Precipitation Over the Atlantic Southern Ocean and Its Impact on Surface Salinity

The DJF climatology of daily mean precipitation occurs as a band crossing the Atlantic sector of the Southern Ocean from the NW to SE (Figure 1a). A strong meridional gradient exists with precipitation weakening over the Southern Ocean (<40°S). This is in accordance with known trends in the spatial distribution of transport over the region (Ramos et al., 2019) and the impact of midlatitude cyclones that track on average in a zonal direction toward the east (Patoux et al., 2009). Similarly, AR climatology (Figure 1b) corresponds with the overall NW to SE tilt of the climatological precipitation (Figure 1a) and observed AR tracks (Ramos et al., 2019). The tilt is also like the mean meridional tilt of the mobile atmospheric fronts in much of the midlatitudes (NW-SE; Simmonds et al., 2012). The climatological means for 54°S, 0°E are 2.43 mm day^{-1} (over 454 km^2) and 2.7% for precipitation and AR presence, respectively.

At the location of the WG deployment (marked in Figures 1a and 1b), precipitation events occur intermittently (6 ± 5 days) as short bursts (12 ± 6 hr) of rainfall (Figure 1d). This concurs with the observed frequency of storms in the region (Swart et al., 2015). Large events (>75th percentile of precipitation) accounted for 88% of the total precipitation observed during the 55 days of WG observations. The WG observations show a seasonal decrease in salinity of ~0.03 g kg^{-1} over the duration of the deployment (Figure 1f), which is primarily due to the accumulated precipitation in the surface ocean over the summer (2.17 ± 3.89 mm day^{-1}, 120 mm total) (Nicholson et al., 2022; du Plessis et al., 2022). We observe large and rapid (<6 hr) responses in salinity during the large rainfall events with four events of salinity decreasing up to 0.05 g kg^{-1} occurring on 27 December 2018, 1 and 5 January, and 7 February 2019 (Figures 1d and 1f). The strongest precipitation event, occurring near the end of the deployment on 6–7 February, resulted in 17 mm of rainfall over a period of 13 hr with a maximum rate of 2 mm hr^{-1}. This resulted in a large observed salinity decrease of 0.37 g kg^{-1}. We use this event to further assess the impact of such rainfall episodes on the surface ocean buoyancy in Section 3.2. Even though precipitation seems to reach the same levels as the event on 6–7 February, it is more likely that the accumulated precipitation during each event plays a bigger part in the strength of the salinity response. The three largest precipitation events (27 December, 19 January, and 7 February) release different amounts of freshwater into the ocean (5.79, 8.15, and 17.0 mm respectively), which are reflected in the varying surface salinity response (0.05, 0.01, and 0.35 g kg^{-1}, respectively) (Figures 1d and 1f). We posit that this could be linked to various processes, such as the active rate of upper-ocean mixing during periods of high wind speed and the extent of the mixed-layer during the different periods of the time series. Using Equation 2 in du Plessis et al. (2022) and assuming that the effects of advection and entrainment are negligible (which do not impact in the same way as precipitation in this region, see Figure 8e, du Plessis et al., 2022), we calculate a mixed-layer salinity budget for the whole time series. Starting with a salinity of 34.11 g kg^{-1}, forcing it with the ERA5 precipitation, and using a mean mixed-layer depth of 100 m (using observations from both Nicholson et al., 2022, and du Plessis et al., 2022), we see a decrease in the salinity of 0.04 g kg^{-1}, compared with the actual observed change of 0.03 g kg^{-1}. The difference between the computed and actual change could be due to active mixing when the mixing-layer depth extends below the base of the mixed layer or the slight variability in the mixed-layer depth during the time series. This further strengthens the argument that this is an area that is, at least during this period, not significantly affected by neither advection nor entrainment.

3.2. Atmospheric River Precipitation Events and Their Impact on Surface Buoyancy

During the WG deployment period, we identified 6 ARs (green vertical shading, Figure 2) and 15 storms (green and gray vertical shading, Figure 2) at the study site (Figure 1). All ARs occurred concurrently with a storm, which cumulatively accounted for 47% of the total precipitation observed during the sampling period. The mean precipitation per storm with an accompanying AR was 9.45 ± 3.68 mm (buoyancy flux of 6.8×10^{-7} m^2 s^{-3}), while storm events without an apparent direct supply of moisture by an AR were characterized by an average of 4.99 ± 2.88 mm of precipitation (buoyancy flux of 3.6×10^{-7} m^2 s^{-3}). This suggests that ARs have the potential to approximately double (189% increase) storm-induced precipitation and surface ocean buoyancy forced by precipitable freshwater.

Cumulative precipitation over the 55 days accounted for 21% of the total surface ocean buoyancy gain with about 10% of the total gain pertaining to AR events (Figure 2d). However, the six largest hourly surface buoyancy fluxes were caused by precipitation (mean buoyancy flux = $1.4 \pm 0.08 \times 10^{-7}$ m^2 s^{-3}), while the surface heat flux-driven buoyancy gain only accounted for two out of the 10 largest buoyancy fluxes ($1.3 \pm 0.01 \times 10^{-7}$ m^2 s^{-3}). The largest buoyancy flux from a precipitation event was 18% larger than the largest buoyancy flux from surface heat fluxes despite being during summer. To compare the relative contribution of precipitation to surface buoyancy gain, we identify the proportion of precipitation (haline)-driven buoyancy gain to the total buoyancy gain (Figure 2e). During large precipitation events, the haline-driven surface buoyancy fluxes exceeded 50% of the total buoyancy flux (e.g., 7 February).

To illustrate the immediate impact of AR-linked precipitation on the surface ocean buoyancy, we investigate the event with the strongest salinity signal (Figure 3). On 6 February at 12:00 UTC, an AR (black, Figures 3a and 3d) was present over the WG site, stretching from about 25.5°S, 24°W to 54°S, 22.5°E, almost 5,000 km. At its maximum IVT (~40°S), it was transporting 4.8×10^8 kg s^{-1} (0.48 Sv) of freshwater across its width (>2 times the mean annual outflow of the Amazon River, Gupta, 2008). The AR connected with the leading edge of a storm

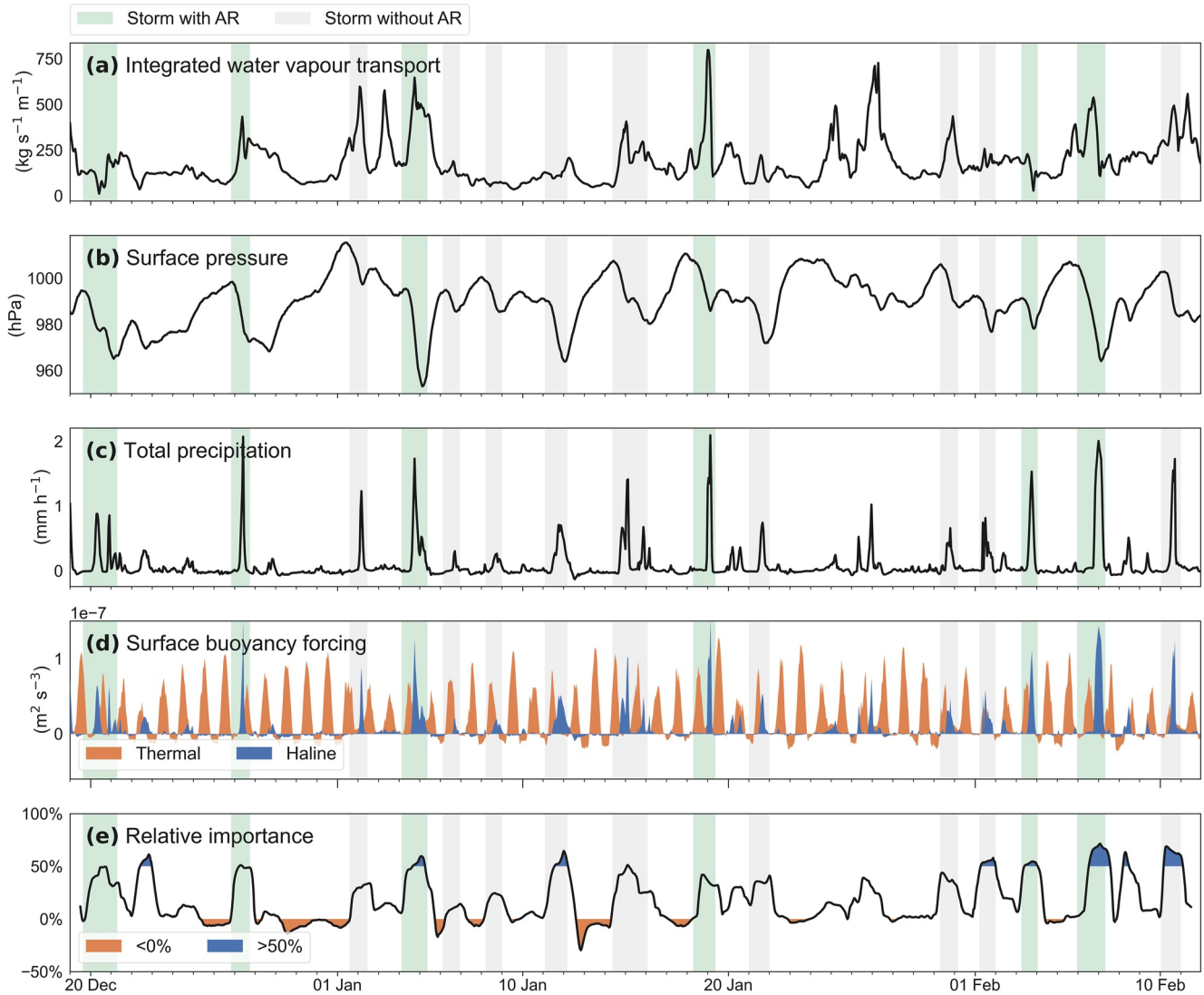

Figure 2. Integrated Water Vapor Transport (a), sea level pressure (b), and total precipitation (c) from ERA5 collocated in space and time to Wave Glider (WG) observations. (d) Thermal and haline components of surface buoyancy forcing derived from ERA5 and observations by the WG. (e) The relative contribution of the haline component to the total surface buoyancy forcing (in percent). Periods when the haline component contributed more than 50% or less than 0% are shaded. These negative percentages indicate periods of evaporation. Vertical bands in all panels highlight the period of a passing storm, and the color determines if an atmospheric river was present (green) or not (gray) during the storm.

south of the study site (black dashed isobars, Figure 3d) with the central low pressure (968 hPa) located at ~58°S, 6°W. The highest area of IVT is located north of the glider with accompanying enhanced levels of precipitation of >3 mm hr^{-1} (white isohyets, Figure 3d). Strong (12 m s^{-1}) northwesterly winds (Figure 3g) were sustained with a salinity of 34.09 g kg^{-1} (Figure 3i) and a thermal buoyancy flux of 7.14×10^{-8} m^2 s^{-3} at the study site (Figure 3j). After 12 hr (00:00 UTC), the storm and the connected AR were directly over the WG (Figure 3e), resulting in the precipitation of 2 mm hr^{-1} (Figure 3h). Concurrently, as the center of the storm passed over the WG, the wind decreased to 4.6 m s^{-1} (at 00:00 UTC, dropping to 1.02 m s^{-1} at 02:10 UTC) and in response to the precipitation, the salinity decreased by 0.37 g kg^{-1} to 33.72 g kg^{-1} (Figure 3i). The haline component dominates the buoyancy flux over the 24 hr surrounding the peak (1.43×10^{-7} m^2 s^{-3}, twice that of the thermal component 12 hr earlier). The maximum rate of precipitation related to the same event 450 km northeast of the study site was 4.4 mm hr^{-1}. At 12:00 UTC, 12 hr later, this feature propagated away from the WG site and is no longer classified as an AR (Figure 3c). After the center of the storm had passed the WG site, the trailing edge of the storm increased the wind to the same magnitude prior to the event (12 m s^{-1}, Figure 3f). Precipitation at the WG

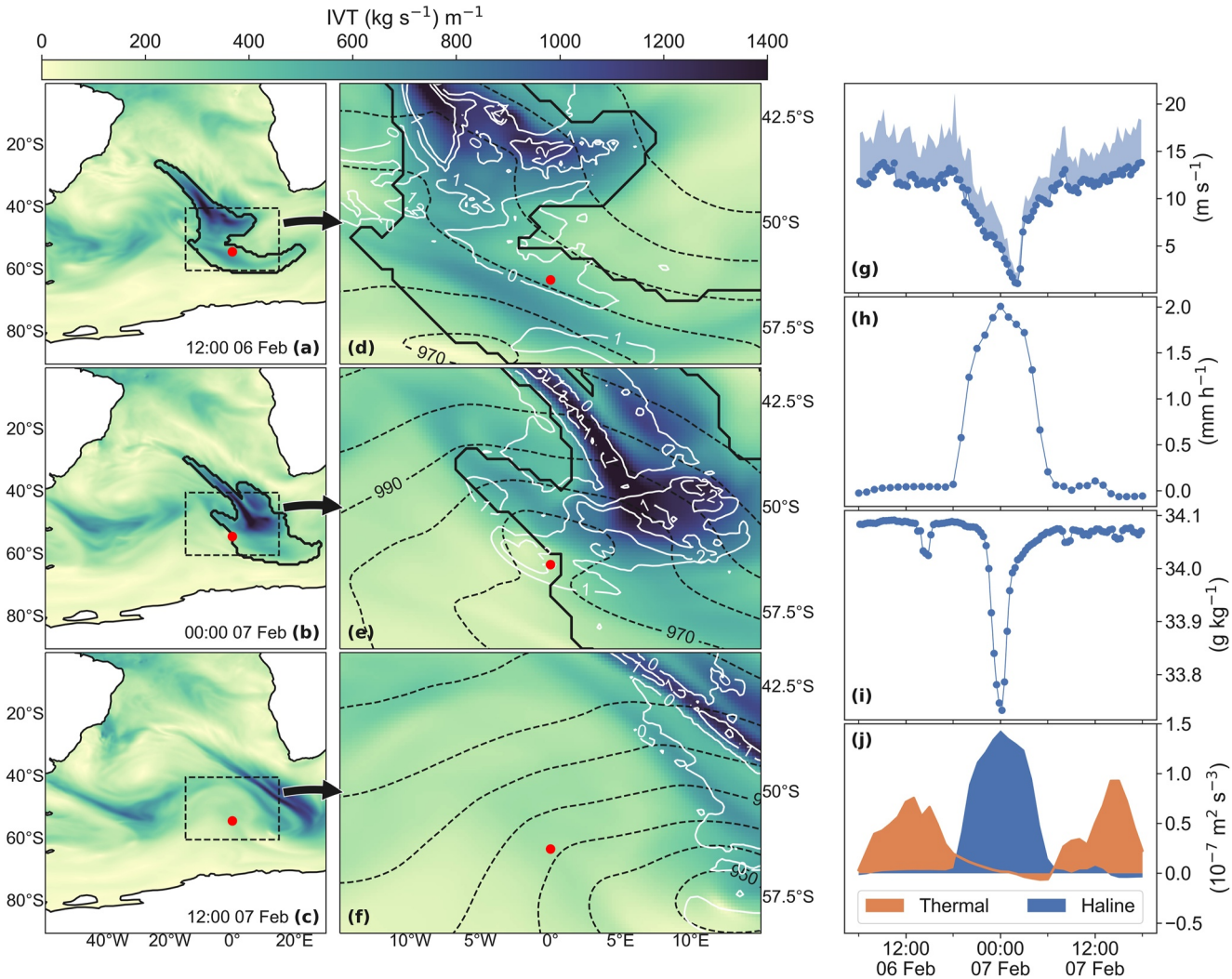

Figure 3. A case study illustrating the surface ocean response to an atmospheric river-linked precipitation event (7 February 2019) as measured by the Wave Glider (WG). (a–f) Snapshots of Integrated Water Vapor Transport (IVT), derived from ERA5 data at three different times: at maximum precipitation for the event and 12 hr before and after. An atmospheric river is marked by black contours in (a, b) and (d, e). (a–c) Large-scale context and spatial extent of IVT over the Atlantic sector of the Southern Ocean. The equivalent "zoomed-in" panels (d–f) are marked with the black-dashed box and the red dot is the WG site in both sets of maps. In (d–f), isobars (dashed black) and isohyets (precipitation, solid white) are added. (g) In situ wind speed and 20-min maximum gusts (m s^{-1}) as measured by the WG, (h) ERA5 precipitation at the WG site, and (i) in situ surface salinity observed by the WG. (j) Haline and thermal contribution to surface buoyancy. The dots in (g–i) represent the temporal resolution, 20 min for the WG data, and hourly for the ERA5 data.

site decreased to 0.1 mm hr^{-1} as the trailing edge of the storm passed over with the observed salinity increasing to values compared prior to the event (34.06 g kg^{-1}), albeit slightly fresher (0.03 g kg^{-1}). A total of 17.0 mm of rain was recorded during the 24 hr period, greater than the 90th percentile of precipitation for the zoomed-in area. The haline buoyancy flux accounted for 53% of the total buoyancy gained. The change in salinity, from 34.09 to 33.72 g kg^{-1}, coupled with the 17.0 mm rain and low wind speeds, would create a low-saline surface layer with a thickness of 1.7 m. The observed rapid increase in salinity once wind stress, and subsequently surface mixing increased, suggests that the precipitation-induced freshwater layer at the surface is rapidly mixed throughout the mixed layer.

4. Discussion

4.1. Effects From AR-Storm Precipitation on Surface Buoyancy Forcing

We show that while surface heating accounts for the majority (79%) of surface ocean buoyancy gain over summer, short-lived precipitation events linked to ARs and storm events can dominate the total buoyancy gained over a 24 hr period (Figure 2e). Our field observations of sea surface salinity indicated that the response to precipitation occurs rapidly (<2 hr) but returns to the near the original salinity usually within 6 hr, albeit slight fresher. This may be a result of the WG being a moving platform, entering an area affected by rain that relates to a decrease in salinity, and then leaving the localized area affected by rainfall-induced surface freshening, raising the salinity once again. Iyer and Drushka (2021) observed such rainfall-induced patchiness in surface salinity as their ship entered an area (~7 km in length) with ongoing precipitation (up to 60 mm hr^{-1}). The salinity at 23 cm, which is the closest to our measurement depth (~30 cm), varied significantly horizontally, up to ±1 PSU at a high frequency in both temporal and spatial space (5–10 min and less than kilometer scale). The distance between our observations (0.74 ± 0.18 m) was close to the spatial scale needed to resolve this patchiness even though higher resolution data would be optimal. Other studies have also observed a similar heterogeneous patchiness of these freshwater pools located on the surface ocean (Moulin et al., 2021; Shcherbina et al., 2019). Shcherbina et al. (2019) observed the formation of a 4-m-thick rain lens at the surface, which eventually was dissipated into the larger water mass within 4 hr from the start of the precipitation. This rapid downward mixing of surface salinity is similar to our observations during 6–7 February, where we estimate a 1.7 m thickness of a surface layer from 2.0 mm hr^{-1} precipitation and 0.37 g kg^{-1} change in salinity, which is close to the thickness in Shcherbina et al. (2019). Their slightly thicker layer is possibly explained by a greater amount of precipitation (23 mm compared to 17 mm) and weaker winds (5 ± 2 m s^{-1} compared to 10 ± 3 m s^{-1}). The surface turbulence can mix out the effects of surface layer freshening by rapidly detraining the fresher water within the deeper mixed layer after a precipitation event, especially in the Southern Ocean with active wind-induced mixing (Nicholson et al., 2022; Swart et al., 2020). This is visible in the full time series wind speed (Figure 1e) when periods of high precipitation and high wind (e.g., 27 December, 5 January, and 19 January) do not produce the same strong signal in salinity as the case study. Concurrent profiling glider observations from this experiment show that despite the mixed-layer depth remaining relatively stable, the mixing-layer depth can vary significantly during storms or strong wind events (see Figure 2, Nicholson et al., 2022). The 2-day mean surface salinity before and after the precipitation event presented in the case study saw a decrease of 0.012 g kg^{-1}, increasing the buoyancy of the surface waters.

Francis et al. (2020) provide further evidence of the role of ARs in the Weddell Sea by relating the effects of ARs on sea ice melt, partly due to oceanic heat gain from the associated moist, warm advected air masses 1,320 km southward of this location. They observed similar precipitation rates to this study (~2 mm hr^{-1}), which are thought to have assisted in the formation of the Weddell polynya in 2017. While Francis et al. (2020) investigate these processes during late winter, this study was conducted during austral summer, when solar radiation is at a maximum (Figure S2 in Supporting Information S1). Thus, the thermal contribution to buoyancy also is at a maximum (Equation 1). The monthly mean precipitation at the study site indicates a maximum during April, in autumn, and a minimum during summer (Figure S2 in Supporting Information S1). Thus, the effect of AR-linked precipitation on the surface ocean buoyancy flux observed in this study is likely to be of a lower order magnitude than at other times of the year. Pellichero et al. (2018) also showed that temperature is the dominant input to the mixed-layer buoyancy during summer in the ice-free open ocean. Therefore, in situ observations extending into winter are needed to further quantify the total input of buoyancy to the surface ocean by ARs.

This study identifies ARs extending from the Subtropics to the high latitudes of the Southern Ocean. Our findings show that ARs are part of a complicated network of synoptic features, all playing a role in regulating surface ocean temperature and salinity budgets in this region of the Southern Ocean. Large midlatitude cyclones are found to be the main supplier of precipitation to the surface ocean with 84% of the total precipitation during the time series being discharged by storms. When connected to storms, ARs significantly increase the precipitation, which can strongly adjust the surface salinity of the ocean, albeit for relatively short periods (6 hr). These events adjust salinity in the mixed layer as the precipitation is dissipated vertically rather than advected horizontally as shown in du Plessis et al. (2022). This contributes to an overall decrease in seasonal salinity over the time series. Given the observed influence of midlatitude cyclones and ARs on the cumulative summer buoyancy gain in the Atlantic sector of the Southern Ocean, we hypothesize that ARs contribute to the buoyancy variability in this sector of the

Southern Ocean on seasonal timescales. Future work is required to investigate the cumulative impacts of ARs on the surface ocean and their possible influence on the Atlantic meridional overturning circulation.

4.2. Caveats of AR-Storm Interactions From an Eulerian Framework

Midlatitude cyclones are the major mechanism in bringing precipitation to the surface ocean, and they provide substantially more precipitation when connected to an AR (189%, Figures 2a–2c). All the identified major storms (15), which passed through our study site (54°S, 0°E) during summer, were associated with high precipitation rates (>75th percentile, Figures 2a–2c), accounting for 84% of the precipitation during this period. As the study site is south of the time-mean AR-storm moisture pathway (Figure 1b), our findings likely represent a lower order contribution of coupled AR-storm impacts on precipitation and thus on the summer mean upper-ocean buoyancy budget. Moreover, a challenge of observing storm-ocean interactions in a quasi-Eulerian framework is that storms are large (∼1,000 km), spatially heterogeneous, and propagate horizontally at relatively rapid speeds (average residency time of a storm during this mission was 25.6 ± 7.1 hr). This means that the edge of a storm system could pass nearby the study site, leading to what appears like a less significant drop in pressure and a "weak" storm, and an underestimation of the impacts of these events on the surface ocean. Similarly, with ARs, the detection algorithm is based on a set of strict co-dependent criteria (Section 2.2), if either criterion fails, then it is not flagged as an AR. This very binary algorithm may lead to moisture being in the area due to a previously classified AR, which then falls as precipitation when a storm passes the area, particularly as ARs are typically found at the leading edge of a storm (Ralph et al., 2017). The occasional high values of IVT in Figure 2a are most likely moisture filaments that are above the threshold of IVT, but do not fit the other criteria, and are therefore not classified as ARs.

Data Availability Statement

The data used in the manuscript are original and can be found here: https://doi.org/10.5281/zenodo.5079732.

Acknowledgments
This study and related data collection were supported by the following grants: Wallenberg Academy Fellowship (WAF 2015.0186), Swedish Research Council (VR 2019–04400), STINT-NRF Mobility Grant and NRF-SANAP (SNA170522231782 and SANAP200324510487). We thank Sea Technology Services (STS), SANAP, and the captain and crew of the S.A. Agulhas II for their fieldwork and technical assistance in Wave Glider deployments and retrievals in the Southern Ocean. We thank Pedro M.S. Monteiro (CSIR-SOCCO) for allowing access to the Wave Glider data set, a major component of the study, and for comments in the manuscript before submission. SS, MdP, and S-AN have received funding from the European Union's Horizon 2020 research and innovation programme under grant agreement N°821001 (SO-CHIC). MdP has been supported by the European Union's Horizon 2020 Marie Skłodowska Curie Individual Fellowship with Project ID 101032683.

References

Abernathey, R. P., Cerovecki, I., Holland, P. R., Newsom, E., Mazloff, M., & Talley, L. D. (2016). Water-mass transformation by sea ice in the upper branch of the Southern Ocean overturning. *Nature Geoscience*, *9*(8), 596–601. https://doi.org/10.1038/ngeo2749

Blamey, R. C., Ramos, A. M., Trigo, R. M., Tomé, R., & Reason, C. J. C. (2018). The influence of atmospheric rivers over the South Atlantic on winter rainfall in South Africa. *Journal of Hydrometeorology*, *19*(1), 127–142. https://doi.org/10.1175/JHM-D-17-0111.1

Cohen, L., Hudson, S. R., Walden, V. P., Graham, R. M., & Granskog, M. A. (2017). Meteorological conditions in a thinner Arctic sea ice regime from winter to summer during the Norwegian Young Sea Ice expedition (N-ICE2015). *Journal of Geophysical Research*, *122*(14), 7235–7259. https://doi.org/10.1002/2016JD026034

Doeschate, A., Sutherland, G., Bellenger, H., Landwehr, S., Esters, L., & Ward, B. (2019). Upper ocean response to rain observed from a vertical profiler. *Journal of Geophysical Research: Oceans*, *124*(6), 3664–3681. https://doi.org/10.1029/2018JC014060

du Plessis, M. D., Swart, S., Biddle, L. C., Giddy, I. S., Monteiro, P. M. S., Reason, C. J. C., et al. (2022). The daily-resolved Southern Ocean mixed layer: Regional contrasts assessed using glider observations. *Journal of Geophysical Research: Oceans*, *127*(4), e2021JC017760. https://doi.org/10.1029/2021JC017760

Francis, D., Mattingly, K. S., Temimi, M., Massom, R., & Heil, P. (2020). On the crucial role of atmospheric rivers in the two major Weddell Polynya events in 1973 and 2017 in Antarctica. *Science Advances*, *6*(46), 1–14. https://doi.org/10.1126/sciadv.abc2695

Gregor, L., Ryan-Keogh, T. J., Nicholson, S. A., du Plessis, M. D., Giddy, I., & Swart, S. (2019). GliderTools: A Python toolbox for processing underwater Glider data. *Frontiers in Marine Science*, *6*(December), 1–13. https://doi.org/10.3389/fmars.2019.00738

Guan, B., & Waliser, D. E. (2015). Detection of atmospheric rivers: Evaluation and application of an algorithm for global studies: Detection of Atmospheric Rivers. *Journal of Geophysical Research: Atmospheres*, *120*(24), 12514–12535. https://doi.org/10.1002/2015JD024257

Gupta, A. (Ed.) (2008). *Large rivers: Geomorphology and management*. *John Wiley & Sons*.

Hersbach, H., Bell, B., Berrisford, P., Hirahara, S., Horányi, A., Muñoz-Sabater, J., et al. (2020). The ERA5 global reanalysis. *Quarterly Journal of the Royal Meteorological Society*, *146*(730), 1–51. https://doi.org/10.1002/qj.3803

Iyer, S., & Drushka, K. (2021). Turbulence within rain-formed fresh lenses during the SPURS-2 experiment. *Journal of Physical Oceanography*, *51*(5), 1705–1721. https://doi.org/10.1175/JPO-D-20-0303.1

Marshall, J., & Speer, K. (2012). Closure of the meridional overturning circulation through Southern Ocean upwelling. *Nature Geoscience*, *5*(3), 171–180. https://doi.org/10.1038/ngeo1391

Moulin, A. J., Moum, J. N., Shroyer, E. L., & Hoecker-Martínez, M. (2021). Freshwater lens fronts propagating as buoyant gravity currents in the equatorial Indian Ocean. *Journal of Geophysical Research: Oceans*, *126*(8), e2021JC017186. https://doi.org/10.1029/2021JC017186

Nash, D., Waliser, D., Guan, B., Ye, H., & Ralph, F. M. (2018). The role of atmospheric rivers in extratropical and polar hydroclimate. *Journal of Geophysical Research: Atmospheres*, *123*(13), 6804–6821. https://doi.org/10.1029/2017JD028130

Nicholson, S. A., Whitt, D. B., Fer, I., du Plessis, M. D., Lebehot, A. D., Swart, S., et al. (2022). Storms drive outgassing of CO_2 in the subpolar Southern Ocean. *Nature Communications*, *13*(1), 158. https://doi.org/10.1038/s41467-021-27780-w

Patoux, J., Yuan, X., & Li, C. (2009). Satellite-based midlatitude cyclone statistics over the Southern Ocean: 1. Scatterometer-derived pressure fields and storm tracking. *Journal of Geophysical Research*, *114*(D4), D04105. https://doi.org/10.1029/2008JD010873

Payne, A. E., Demory, M.-E., Leung, L. R., Ramos, A. M., Shields, C. A., Rutz, J. J., et al. (2020). Responses and impacts of atmospheric rivers to climate change. *Nature Reviews Earth & Environment*, *1*(3), 143–157. https://doi.org/10.1038/s43017-020-0030-5

Pellichero, V., Sallée, J. B., Chapman, C. C., & Downes, S. M. (2018). The southern ocean meridional overturning in the sea-ice sector is driven by freshwater fluxes. *Nature Communications*, *9*(1), 1–9. https://doi.org/10.1038/s41467-018-04101-2

Ralph, F. M., Dettinger, M., Lavers, D., Gorodetskaya, I. V., Martin, A., Viale, M., et al. (2017). Atmospheric rivers emerge as a global science and applications focus. *Bulletin of the American Meteorological Society*, *98*(9), 1969–1973. https://doi.org/10.1175/BAMS-D-16-0262.1

Ramos, A. M., Blamey, R. C., Algarra, I., Nieto, R., Gimeno, L., Tomé, R., et al. (2019). From Amazonia to southern Africa: Atmospheric moisture transport through low-level jets and atmospheric rivers. *Annals of the New York Academy of Sciences*, *1436*(1), 217–230. https://doi.org/10.1111/nyas.13960

Savitzky, A., & Golay, M. J. E. (1964). Smoothing and differentiation of data by simplified least squares procedures. *Analytical Chemistry*, *36*(8), 1639–1643. https://doi.org/10.1021/ac60214a047

Schmidt, K. M., Swart, S., Reason, C. J. C., & Nicholson, S. A. (2017). Evaluation of satellite and reanalysis wind products with in situ wave glider wind observations in the southern ocean. *Journal of Atmospheric and Oceanic Technology*, *34*(12), 2551–2568. https://doi.org/10.1175/JTECH-D-17-0079.1

Shcherbina, A. Y., D'Asaro, E. A., & Harcourt, R. R. (2019). Rain and sun create slippery layers in the eastern Pacific fresh pool. *Oceanography*, *25*(3), 56–67. https://doi.org/10.5670/oceanog.2011.65

Shields, C. A., Rutz, J. J., Leung, L.-Y., Ralph, F. M., Wehner, M., Kawzenuk, B., et al. (2018). Atmospheric river tracking method intercomparison project (ARTMIP): Project goals and experimental design. *Geoscientific Model Development*, *11*(6), 2455–2474. https://doi.org/10.5194/gmd-11-2455-2018

Simmonds, I., Keay, K., & Bye, J. A. T. (2012). Identification and climatology of Southern Hemisphere mobile fronts in a modern reanalysis. *Journal of Climate*, *25*(6), 1945–1962. https://doi.org/10.1175/JCLI-D-11-00100.1

Sousa, P. M., Blamey, R. C., Reason, C. J. C., Ramos, A. M., & Trigo, R. M. (2018). The "Day Zero" Cape Town drought and the poleward migration of moisture corridors. *Environmental Research Letters*, *13*(12), 124025. https://doi.org/10.1088/1748-9326/aaebc7

Swart, S., Chang, N., Fauchereau, N., Joubert, W., Lucas, M., Mtshali, T., et al. (2012). Southern Ocean Seasonal Cycle Experiment 2012: Seasonal scale climate and carbon cycle links. *South African Journal of Science*, *108*(3–4), 3–5. https://doi.org/10.4102/sajs.v108i3/4.1089

Swart, S., du Plessis, M. D., Thompson, A. F., Biddle, L. C., Giddy, I., Linders, T., et al. (2020). Submesoscale fronts in the Antarctic marginal ice zone and their response to wind forcing. *Geophysical Research Letters*, *47*(6), 1–10. https://doi.org/10.1029/2019GL086649

Swart, S., Thomalla, S. J., & Monteiro, P. M. S. (2015). The seasonal cycle of mixed layer dynamics and phytoplankton biomass in the Sub-Antarctic Zone: A high-resolution glider experiment. *Journal of Marine Systems*, *147*, 103–115. https://doi.org/10.1016/j.jmarsys.2014.06.002

Wang, Z., Siems, S. T., Belusic, D., Manton, M. J., & Huang, Y. (2015). A climatology of the precipitation over the Southern Ocean as observed at Macquarie Island. *Journal of Applied Meteorology and Climatology*, *54*(12), 2321–2337. https://doi.org/10.1175/JAMC-D-14-0211.1

Wille, J. D., Favier, V., Gorodetskaya, I. V., Agosta, C., Kittel, C., Beeman, J. C., et al. (2021). Antarctic atmospheric river climatology and precipitation impacts. *Journal of Geophysical Research: Atmospheres*, *126*(8), e2020JD033788. https://doi.org/10.1029/2020jd033788

Zhang, Z., Ralph, F. M., & Zheng, M. (2019). The relationship between extratropical cyclone strength and atmospheric river intensity and position. *Geophysical Research Letters*, *46*(3), 1814–1823. https://doi.org/10.1029/2018GL079071

Zhu, Y., & Newell, R. E. (1998). A proposed algorithm for moisture fluxes from atmospheric rivers. *Monthly Weather Review*, *126*(3), 725–735. https://doi.org/10.1175/1520-0493(1998)126<0725:APAFMF>2.0.CO;2